Acta Polytechnica **65**(4):406–419, 2025
https://doi.org/10.14311/AP.2025.65.0406

Published by the Czech Technical University in Prague

IMPROVING THE PRODUCTION PROCESS OF SILICON NANOPARTICLE AND QUARTZ MICROLENS

Muaath J. Mahmoud[a,*], Bassam G. Rasheed[b], Muammel M. Hanon[c,†]

[a] *Scientific Research Commission, Jadriyah, 10070 Baghdad, Iraq*

[b] *Al-Nahrain University, College of Engineering, Laser & Optoelectronics Engineering Department, Jadriyah, 10072 Baghdad, Iraq*

[c] *Middle Technical University, Baquba Technical Institute, Muasker Al Rashid Street, 10074 Baghdad, Iraq*

[*] corresponding author: muaathjamal@yahoo.com

[†] corresponding author: muammel.m.hanon@mtu.edu.iq

Abstract. This study presents a comprehensive investigation into advanced laser micro/nano machining techniques, utilising three distinct laser sources: a Q-switched Nd:YAG laser, a fibre laser, and a CO_2 laser. Notably, the creation of remarkably stable silicon nanoparticles was achieved, opening up promising avenues for new applications. The potential of quartz sheets was exploited to produce spherical microlens arrays, thereby demonstrating the precision of optical element engineering. The distribution of surface and subsurface temperatures for both silicon and quartz materials during laser processing was determined through an in-depth thermal analysis facilitated by COMSOL software. Notably, peak temperatures of 5 700 K and 2 630 K were achieved for silicon and quartz, respectively, highlighting the effectiveness of the laser methodologies employed. Numerical optimisations were conducted using Design of Experiments (DOE) software to enhance silicon nanoparticle production, yielding nanoparticles with a remarkable stability parameter of 33.5 mV. Furthermore, notable outcomes were achieved in the production of quartz microlenses with a numerical aperture of 0.494 and a surface roughness of 4.5 nm. The controllable and precise nature of the laser micro/nano machining techniques enables applications in optoelectronics and advanced biological imaging. The exceptional properties of the engineered silicon nanoparticles and microlens arrays demonstrate their potential across various scientific and technological domains.

Keywords: Quartz microlens, silicon nanoparticles, laser microprocessing, box Behnken design, ANOVA analysis.

1. Introduction

Over the past decade, there has been significant attention and research efforts surrounding the laser microprocessing of brittle materials, including glass, ceramics, and semiconductors [1]. This pivotal technology is crucial in producing precise parts and components used across various industries, such as electronics, optoelectronics, and aerospace engineering [2]. One of the challenges in laser microprocessing of brittle materials is the tendency of these materials to crack and fracture under stress [3]. This can occur due to thermal stress generated by heat from laser absorption, as well as mechanical stress. To minimise the risk of cracking and other forms of damage, laser parameters, such as pulse duration, intensity, and wavelength, must be carefully chosen [4].

Silicon has been extensively studied due to its critical role in modern electronics and semiconductor applications [5]. It serves as a fundamental substrate material for various electronic devices. In both solar cells and other semiconductor components, crystalline and amorphous silicon are widely used [6]. Silicon nanoparticles (NPs) are also widely used in photovoltaics, optoelectronics, biomedical applications, and energy storage due to their environmentally friendly nature, high surface-area-to-volume ratio, tunable optical properties, and biocompatibility [7]. However, they are susceptible to oxidation, present synthesis challenges, and exhibit low electrical conductivity. On the other hand, glass microstructures are used in many fields, such as biomedicine, biochemistry, lab-on-a-chip devices, sensors, and hydrophobic applications, glass machining, therefore, attracts much attention [8]. There is a significant demand for high-tech macro products for applications in biotechnology, microelectronics, telecommunications, microelectromechanical systems (MEMS), and medical sector. Quartz microlenses, in particular, play a vital role in fibre optic communications, imaging and sensing, laser processing, and lithography due to their broad optical transmission (UV to IR), high thermal stability, and low optical loss. Despite these advantages, their widespread adoption is sometimes hindered by the complexity of production, high production costs, and the material brittleness [9].

Response surface methodology (RSM) is also known as the Box-Wilson Methodology. Surface methodology responses are a set of statistical and mathematical

Name	Symbol	Range			Unit
		Nd:YAG laser	Fiber laser	CO_2 laser	
Wavelength	λ	1 064 nm	1 064 nm	10.6 µm	nm
Energy	E	0.1–2	-	-	J
Beam diameter	D	1	0.1	2	mm
Pulse duration	τ	10	130	-	ns
Repetition rate	R	6	30 000	-	Hz
Power	P	-	0.1–30	0.1–100	W
Laser speed	s	-	10–1 000	1–6	$mm\,s^{-1}$
Operation mode	O	pulse	pulse	CW	-

TABLE 1. Laser parameters.

techniques used to model and analyse problems for which the answer is influenced by a variety of variables. The RSM ties a response or result variable (output) to the data (input) that influences it. If an area with an ideal response is discovered, the model is modified to connect to that area so that the analysis can be performed to determine the optimal area. The RSM must be used in the correct sequence according to the method used [10].

Tewari et al. [11] investigated the quality of holes in laser-drilled kenaf/high-density polyethylene composites by measuring the kerf taper angle, the size of the heat-affected zone, and the surface roughness. They used microwave-assisted compression moulding to create composites with 20 wt. % kenaf fibre and investigated the effects of laser power and cutting speed. A central composite design produced a minimum kerf taper of 0.056° and a surface roughness of 3.83 ± 0.19 µm at 120 W and $2\,mm\,s^{-1}$. A regression model demonstrated a high level of agreement with the experimental data, with errors of less than 5.35 %, validating the method's suitability for precision machining. Theeda et al. [12] studied industrial ultrafast lasers with pulse durations ranging from 300 fs to 10 Ps, powers of up to 150 W, and pulse energy of 10–250 µJ for precision micro-machining. Their research examines the influence of major laser settings on machining speed and quality. It provides recommendations for optimisation based on experimental data for 25 materials. Furthermore, they examine the ultrafast laser business and its industrial uses. Zheng et al. [13] investigated the use of picosecond laser for drilling carbon-fibre reinforced polymer machining and found that it outperformed existing approaches in terms of reducing heat-affected zones and improving the hole quality. Using the RSM, they optimised laser parameters, attaining a hole wall taper of 4.160° and a HAZ of 18.577 µm. Experimental validation showed negligible variance, proving the technique's industrial viability for high-tech applications.

In this paper, the experimental and theoretical investigations were carried out to optimise the laser micro/nano processing of brittle materials by applying three lasers to silicon and quartz substrates to synthesise silicon nanoparticles and produce quartz microlens. Additionally, incorporating Box Behnken design and ANOVA analysis together with Design of Experiments (DOE) software offers a unique and systematic approach to optimising the production of silicon nanoparticles and quartz microlenses [14]. This comprehensive methodology not only expands the understanding of the underlying processes but also enables precise control over the final properties of the synthesised nanoparticles and microlens arrays, thus paving the way for more efficient and tailored applications in optoelectronics and biological imaging.

2. Experimental methodology

A Q-switched Nd:YAG laser (1 J pulse laser, China) was used on a pure p-type <100> silicon wafer with dimensions of 20 mm × 20 mm × 500 µm. The fibre (SM-30W, China) and CO_2 lasers (CO_2 laser work station, PI MICOS, Germany) were used on a quartz sheet with dimensions of 10 mm × 10 mm × 1.1 mm in the first and second stages, respectively. All laser parameters are given in Table 1. Before commencing any processing procedures, the silicon wafer and quartz sheets were cleaned in an ultrasonic bath using an ultrasonic device, using ethanol and distilled water as cleaning agents. Ethanol was selected for cleaning the silicon wafer due to its effectiveness in ensuring the required surface cleanliness while providing a milder cleaning method. Its rapid evaporation helps minimising water-related contamination and defects, making it a suitable choice for precision cleaning. Although Radio Corporation of America (RCA) cleaning is commonly used to remove both organic and inorganic contaminants, ethanol was preferred for its efficiency in eliminating organic residues and its ease of handling.

Laser ablation is a process involving the expulsion of material as a result of the generation of a significantly elevated vapour pressure [7]. Laser ablation of solid targets in liquids (LAL) is a very effective way to make nanoparticles because it is easy to control and does not harm the environment. It provides significant protection against potential contamination during the production of nanoparticles [15]. The pulse laser ablation in liquid (PLAL) process successfully synthesised silicon nanoparticles in an

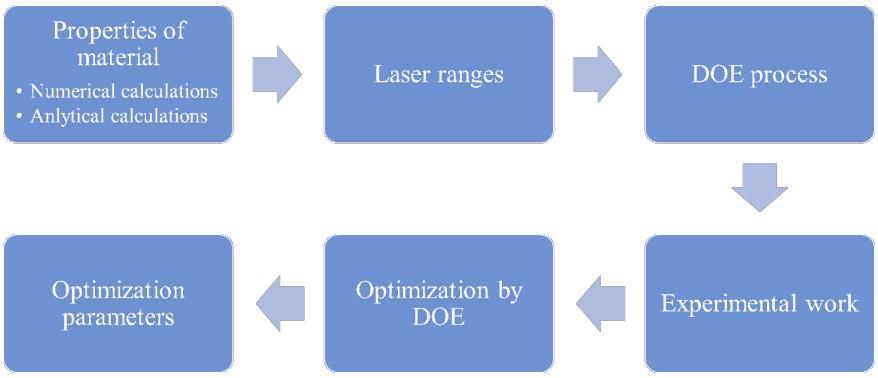

Figure 1. Optimisation procedure for silicon nanoparticles and quartz microlens.

Nd:YAG laser		Fiber laser		CO_2 laser	
Energy [J]	**Silicon Surface Temp. [K]**	**Power [W]**	**Quartz Surface Temp. [K]**	**Power [W]**	**Quartz Surface Temp. [K]**
0.1	569	1	190	1	415
0.2	1 137	4	760	2	825
0.4	2 275	7	1 320	4	1 650
0.6	3 411	13	2 480	6	2 480
0.8	4 548	19	3 590	8	3 300
1	5 685	22	4 150	10	4 130

Table 2. The surface temperature of silicon wafers and quartz sheets depending on the applied laser.

aqueous medium through a two-step procedure. Initially, the silicon wafer was carefully positioned within a plastic container, which was subsequently filled with a precise volume of 2.5 millilitres of deionised water (DW). Next, the wafer was subjected to a controlled exposure of 300 laser pulses. In the subsequent stage, the suspension underwent exposure to a fibre laser for 10 minutes, producing reduced-size silicon nanoparticles. The production of quartz microlenses involved a two-step procedure. Firstly, a fibre laser with a galvanometer system was used to selectively eliminate material from the sheet's surface with predetermined laser parameters. The subsequent stage involves using a CO_2 laser beam to modify the surface of the quartz sheet, resulting in the formation of polished, spherical microlenses. The high-resolution optical microscope (OLYMPUS BX60M) was used to analyse the interaction between the silicon wafer and the quartz sheet. The acquired optical microscope images were then stored, and the dimensions of the produced microlenses were measured using the ImageJ software. The absorption spectrum in the 300–700 nm wavelength range was conducted using an optical absorption spectrometer (Metrech SP8001). Finally, the residual colloidal solution was transferred to a quartz tube for zeta potential analysis silicon NP stability using (Brookhaven-USA).

3. Results and discussion

A comprehensive examination of the fabricated silicon nanoparticles and microlenses involved both empirical investigation and mathematical models.

The procedures of all steps are shown in Figure 1. The first one is related to the material (silicon and quartz) properties, and calculating the temperature generated at the surface and beneath the surface of each material when a laser is applied. After setting the laser range and other parameters in the DOE software, the experimental began, during which the optimisation process in the software took place. In the final step, the optimisation parameters were determined for future processing.

3.1. Theoretical calculations

The material is heated, melted, and evaporated when the laser beam is applied because the target's surface absorbs the energy of the laser [16]. The melting point of silicon is 1 687 K, while its vaporisation point is 3 538 K [17]. According to measurements, the melting and vaporisation points of quartz are 1 923 K and 2 503 K, respectively [18]. The high energy density of the laser causes the surface temperatures of silicon and quartz to rapidly raise after just a brief moment of exposure to the laser beam. The surface temperature for each material can be calculated theoretically using the relationship [19]:

$$T = \frac{\alpha \times F \times A}{p \times c_p}, \tag{1}$$

where α is the absorption coefficient [cm^{-1}], F is the energy density [$\mathrm{W\,A}^{-1}$], A is the absorptivity [$\frac{\text{litres}}{\text{mole cm}}$], p is the density, and c_p is the specific heat [$\mathrm{J\,kg}^{-1}\,^{\circ}\mathrm{C}^{-1}$]. Table 2 presents the relationship between the laser energy/power and surface temperature

for silicon and quartz, derived from theoretical calculations using Equation (1), where the laser energy varies in order to determine the corresponding surface temperature.

In order to theoretically model the laser's interaction with the silicon and quartz, the COMSOL 6.1 program was used [20]. Figure 2 displays the geometry and mesh for each model. Figure 2a shows the silicon wafer geometry with a point heat source in the centre (Nd:YAG laser source) with mesh parameters: maximum element size, minimum element size, maximum element growth rate, curvature factor, and the resolution of the narrow region: 7.0×10^{-5}, 3×10^{-6}, 1.35, 0.3, and 0.85, respectively. Moreover, Figure 2b depicts the quartz wafer geometry with a point heat source in the centre (fibre laser source) with mesh parameters: maximum element size, minimum element size, maximum element growth rate, curvature factor, and the resolution of the narrow region: 5×10^{-5}, 5×10^{-6}, 1.3, 0.2, and 1, respectively. Figure 2c displays the quartz wafer geometry with a point heat source in the centre (CO_2 laser source) with mesh parameters: maximum element size, minimum element size, maximum element growth rate, curvature factor, and the resolution of the narrow region: 4×10^{-5}, 4×10^{-6}, 1.3, 0.2, and 1, respectively.

Surface and sub-surface temperatures are simulated in the model for silicon and quartz, as shown in Figure 3.

Figures 3a, 3c and 3e show the temperature of silicon and quartz at different time intervals (1 ns, 0.1 s, and 0.1 s) for Nd:YAG, fibre, and CO_2 lasers, respectively. As illustrated in Figure 3, the temperature of the silicon surface is approximately 5 700 K. In contrast, the temperature of the quartz surface is approximately 2 630 K for the fibre laser and 2 140 K for the CO_2 laser, as shown in Figures 3a, 3c and 3e.

Due to silicon's strong absorption rates of 1 064 nm, it requires low energy with a short time to achieve the ablation process. This occurs because the laser energy used in the experiment is comparable to the bandgap energy of silicon (1.12 eV), which enables the excitation of electrons from the valence band to the conduction band. As a result, increased absorption, photocarrier generation, and material modifications take place, facilitating the ablation process. In contrast, quartz has a low absorption rate of 1 064 nm, requiring higher power and a longer duration for ablation. Unlike the CO_2 laser/quartz interaction, where the laser power is sufficient to heat the quartz due to its strong absorption of 10.6 µm [21].

Figures 3b, 3d and 3f show that the Nd:YAG and fibre lasers immediately heated the surface and the area beneath it immediately, whereas the CO_2 laser operating continuously heated the entire quartz surface and the area beneath it over a longer period.

In addition, as illustrated in Table 3, the surface temperature of each material at various time points was determined by executing the model in the COMSOL software. The results indicate that laser microprocessing begins instantly when lasers are applied to silicon and quartz surface areas.

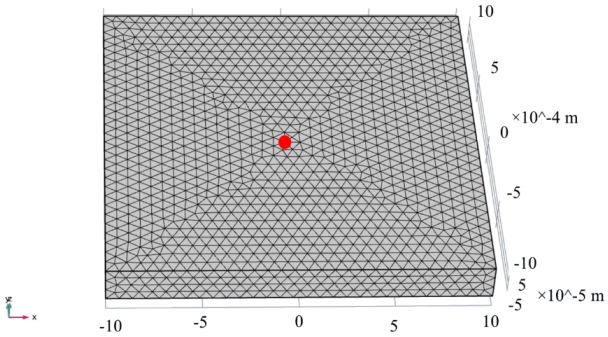

(A). Silicon irradiated by Nd:YAG laser.

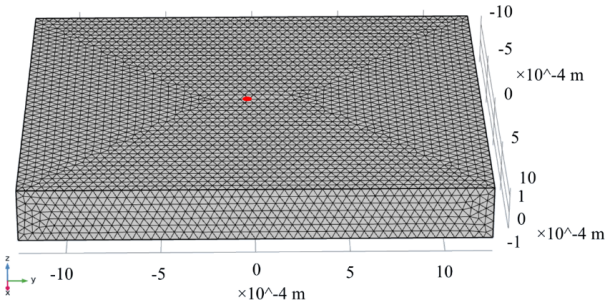

(B). Quartz irradiated by fibre laser at first stage.

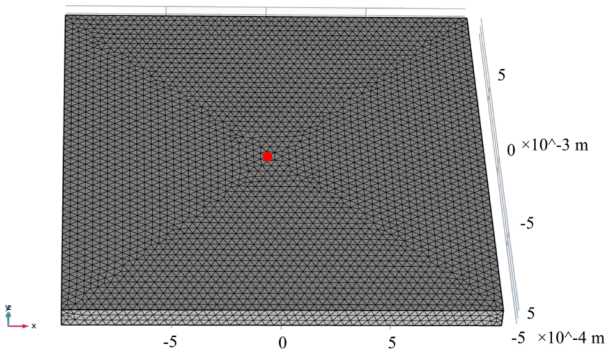

(C). Quartz irradiated by CO_2 laser at final stage.

FIGURE 2. The model geometry, mesh, and heat source for materials irradiated by lasers.

3.2. The irradiation area

Figure 4 shows the irradiation areas of a silicon wafer that were irradiated using an Nd:YAG laser and a quartz sheet that was first irradiated using a fibre laser and then using a CO_2 laser. The observation has revealed that the shape of the interaction region on the silicon surface exhibits a remarkable resemblance to a sphere. As depicted in Figure 4a, the diameter of the interaction area is 800 µm. The interaction area for quartz, as depicted in Figure 4b, exhibits spherical morphologies with a diameter of 200 µm. The variation in diameter among the shapes can be attributed to the disparity in the spot size for each laser type. The Nd:YAG laser has a spot size of 2 mm, while the fibre laser has a spot size of 0.1 mm.

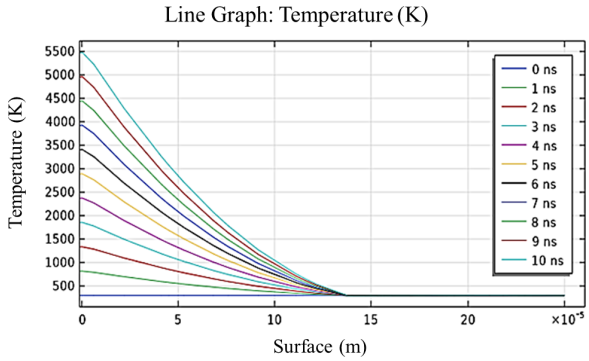

(A). Thermal distribution at the surface of Si.

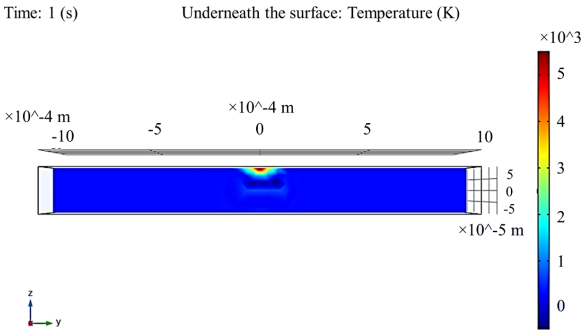

(B). Sub-surface temperature of Si.

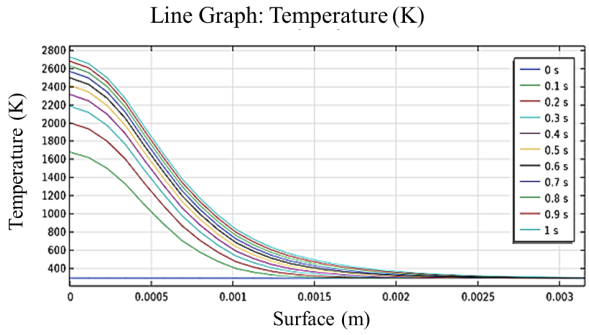

(C). Thermal distribution at the surface of quartz.

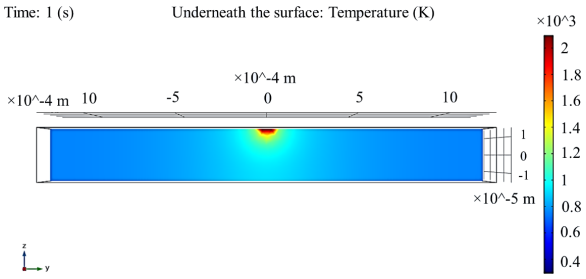

(D). Sub-surface temperature of quartz at first stage.

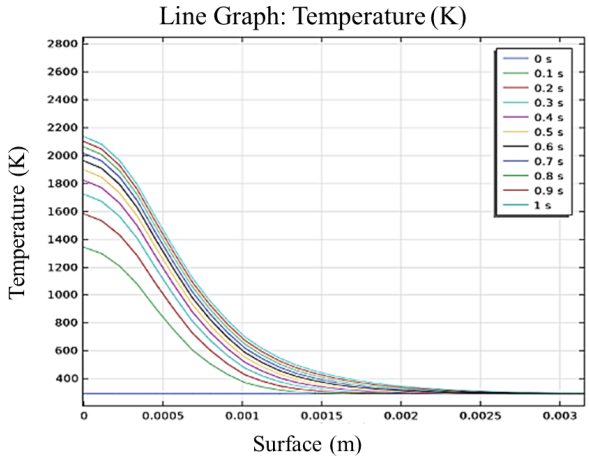

(E). Thermal distribution at the surface.

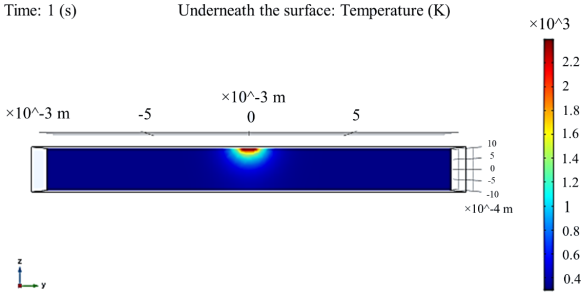

(F). Sub-surface temperature of quartz at second stage.

FIGURE 3. The theoretical model of silicon and quartz irradiated by Nd:YAG laser and fibre laser, followed by CO_2 laser, respectively.

Silicon		**Quartz**		
Nd:YAG laser			**Fiber laser**	**CO_2 laser**
Time [ns]	**T_{max} [K]**	**Time [s]**	**T_{max} [K]**	**T_{max} [K]**
1	835	0.1	2 200	1 345
2	1 377	0.2	2 250	1 600
3	1 919	0.3	2 300	1 725
4	2 460	0.4	2 350	1 825
5	3 002	0.5	2 400	1 900
6	3 544	0.6	2 450	1 960
7	4 049	0.7	2 500	2 015
8	4 626	0.8	2 545	2 060
9	5 166	0.9	2 590	2 100
10	5 700	1	2 630	2 140

TABLE 3. Silicon and quartz maximum surface temperature as a function of time.

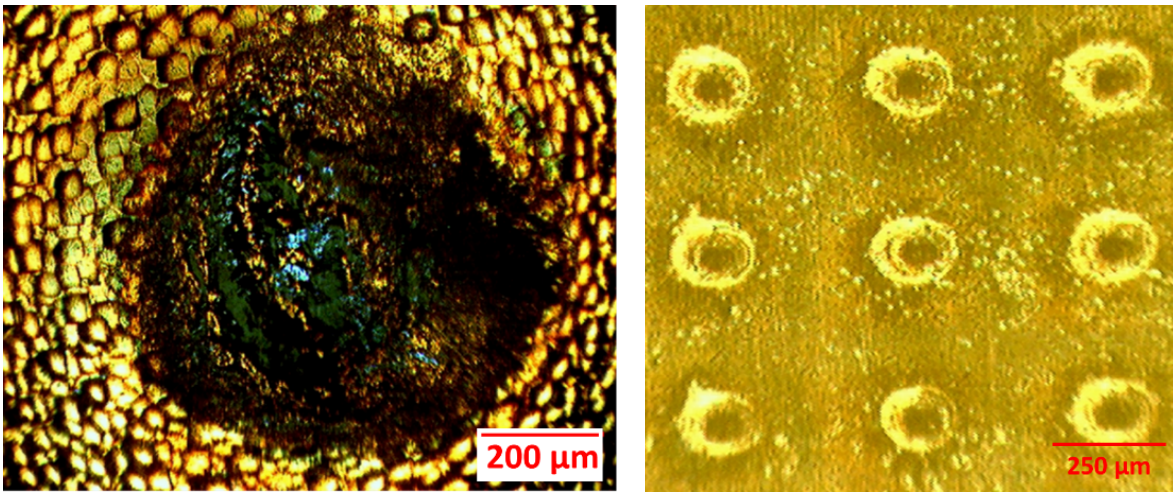

(A). Silicon. (B). Quartz.

FIGURE 4. The optical microscope image of the interaction area of: silicon and quartz.

3.3. STATISTICAL ANALYSIS AND NUMERICAL OPTIMIZATION

The box Behnken design (BBD) was used to investigate the effects of three independent input variables [22], energy, pulse rate, and pulse width of an Nd:YAG laser on a silicon wafer. Additionally, a quartz sheet was used to determine the impact of laser intensity, exposure time, and speed, which are input parameters of a fibre laser, followed by a CO_2 laser for the first and second stages.

The effect of various input parameters on the output parameters was analysed using an ANOVA. Different input parameters were used to measure various results in each experiment to make an error-free mathematical model that connects input variables to outcome responses. The response was predicted using a general quadratic equation for varying amounts of each constituent, as shown by [23]:

$$y = \gamma_o + \sum_{i=1}^{n} \gamma_i x_i + \sum_{i=1}^{n} \gamma_{ii} x_i^2 + \sum_{i} \sum_{j} \gamma_{ij} x_i x_j + E, \tag{2}$$

where γ_o is a constant number, n is the parameter number, γ_i is a linear coefficient, γ_{ii} is a quadratic coefficient, γ_{ij} is a coefficient of laser-material interaction, and E is the parameter error.

The optimisation process includes the combination of various components that were used in combination [24]. The utilisation of numerical optimisation holds significant importance within the Design of Experiments (DOE) software domain [25, 26].

3.4. SILICON NANOPARTICLES

According to the experimental plan in Tables 4 and 5, silicon nanoparticles were subjected to many tests using the Design Expert 12 software. The Design of Experiments (DOE) approach is a valuable tool in engineering research, as it systematically determines optimal values by analysing the relationship between the input and output parameters. The first step involves selecting the input parameters and defining their respective ranges. The software then arranges these parameters using a specific algorithm, allowing for a structured experimental design. In the experimental step, the corresponding output parameters are obtained and recorded based on the arranged input values.

Table 4 presents the experimental results for silicon nanoparticles, where the input parameters include the laser energy, the number of pulses, and the pulse repetition rate (PRR). The lower and upper values for laser energy are 100 and 500 mJ, respectively, while the number of laser pulses ranges from 10 to 90. Similarly, the PRR values range from 1 to 5 Hz. The output parameters measured are the peak wavelength and the absorption peak. This structured experimental design ensures a comprehensive analysis of the relationship between the laser parameters and the silicon nanoparticles. The graphical representation of Table 4 is shown in Figure 5 and Figure 6.

Figure 5 shows a three-dimensional graph of the peak wavelength at 1–5 PRR. The max. and min. peaks were 396 and 327 nm, respectively. Increased laser energy resulted in the creation of smaller silicon nanoparticles, most likely due to more intense ablation dynamics and greater energy densities that promote finer fragmentation of the material. Additionally, a blue shift was observed.

Figure 6 shows a three-dimensional graph of the absorption peak at 1–5 PRR. The max. and min. absorption peaks were 0.389 and 0.038, respectively. An increase in the number of laser pulses leads to a higher concentration of silicon nanoparticles in the suspension, as repeated irradiation enhances the ablation rate and cumulative material removal. This elevated nanoparticle concentration contributes to stronger op-

Run	Input parameters			Output parameters	
	A: Energy [mJ]	B: No. of Pulses	C: PRR [Hz]	Wavelength [nm]	Absorbance
1	500	50	5	332	0.237
2	300	50	3	364	0.151
3	100	50	5	381	0.091
4	500	90	3	331	0.389
5	300	50	3	365	0.156
6	100	50	1	396	0.089
7	300	10	5	388	0.164
8	300	50	3	365	0.156
9	300	10	1	376	0.038
10	300	50	3	367	0.160
11	300	90	5	342	0.312
12	100	90	3	356	0.221
13	500	10	3	327	0.056
14	500	50	1	346	0.226
15	100	10	3	376	0.039
16	300	50	3	367	0.152
17	300	90	1	362	0.291

Table 4. Effects of laser energy, the number of pulses, and (PPR) on the peak wavelength and absorption as determined by the DOE software.

Run	Input parameters			Output parameter
	A: Time [month]	B: Energy [mJ]	C: No. of Pulses	Zeta Potential [mV]
1	2	300	500	19.08
2	2	100	100	31.43
3	1	200	500	27.21
4	2	200	300	25.65
5	1	200	100	32.72
6	3	300	300	20.45
7	1	300	300	27.76
8	2	300	100	24.29
9	3	100	300	22.6
10	2	200	300	25.61
11	2	200	300	25.68
12	3	200	500	20.09
13	2	200	300	25.64
14	1	100	300	32.51
15	3	200	100	24.03
16	2	200	300	25.62
17	2	100	500	25.6

Table 5. Effects of aging time, laser energy, and the number of pulses on the stability as determined by the DOE software.

tical absorption within the medium, due to increased scattering and interaction of the laser beam with the suspended particles.

The quadric equation that should be used to evaluate the peak wavelength (λ) and absorption (A) of silicon nanoparticles, as shown below:

$$\begin{aligned}\lambda = {} & 399.117 + 0.0081E + 0.2828N \\ & + (-11.1875)R + 0.0008E \times N \\ & + 0.0006E \times R + (-0.1)N \times R \\ & + (-0.0003)E^2 + (-0.0045)N^2 + 2.2813R^2,\end{aligned} \tag{3}$$

$$\begin{aligned}A = {} & -0.0201 + 0.0002E + 0.0005N + 0.0024R \\ & + 4.7187 \times 10^{-6} \times E \times N \\ & + 5.625 \times 10^{-6} \times E \times R + (-0.0003)N \times R \\ & + (-2.5312) \times 10^{-7} \times E^2 \\ & + 1.898 \times 10^{-5} \times N^2 + 0.0037R^2,\end{aligned} \tag{4}$$

where E is the laser energy [J], N is the No. of laser pulses, and R is PRR [Hz].

The final regression equations were also an excellent way to predict and study how the parameters affect each other.

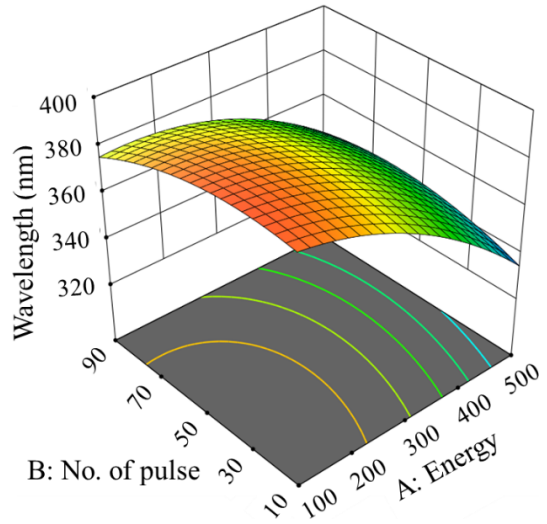

(A). PRR: 1.

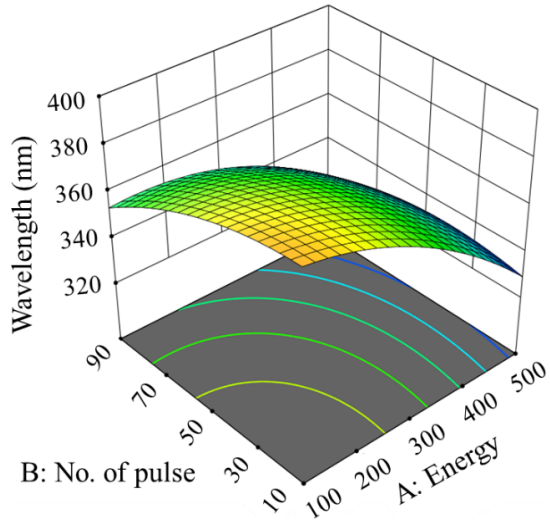

(B). PRR: 3.

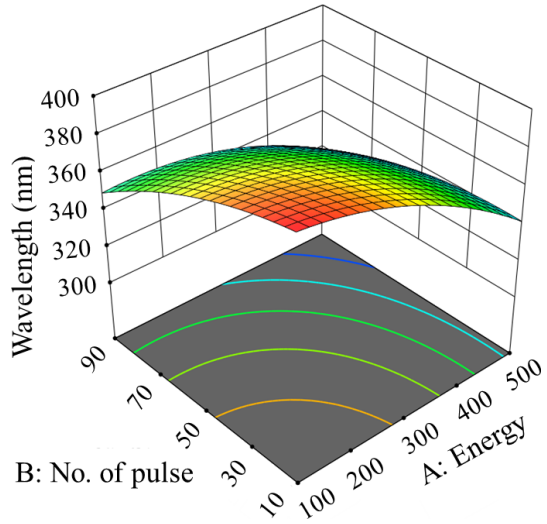

(C). PRR: 5.

FIGURE 5. The wavelength peak curve for No. of pulses and energy at PRR: 1, 3, and 5.

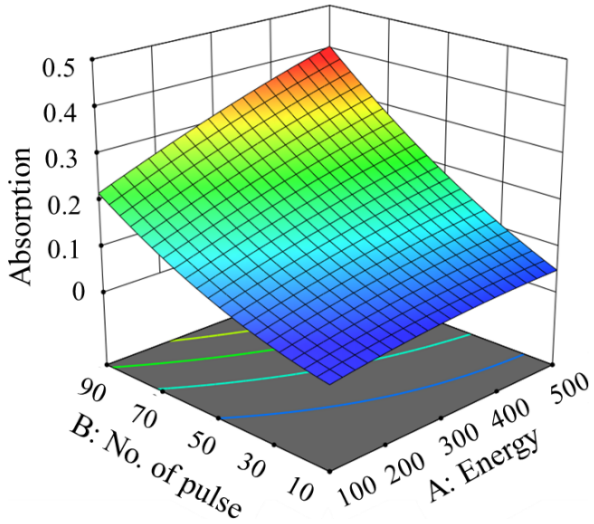

(A). PRR: 1.

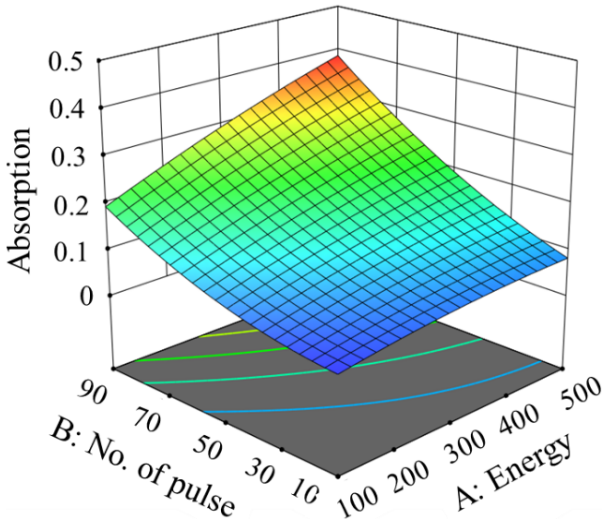

(B). PRR: 3.

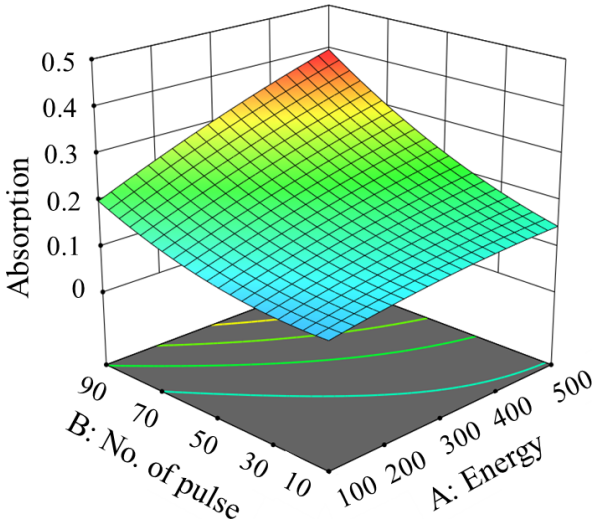

(C). PRR: 5.

FIGURE 6. The absorption peak curve for energy and No. of pulses at PRR: 1, 3, and 5.

The optimum values of the output parameters for Table 4 are shown in Figure 7.

Figure 7 illustrates the optimal values of the output response for Si NPs. When using the Nd:YAG laser, it was observed that the optimal wavelength for peak absorption was 318.5 nm, with a corresponding absorption value of 0.389.

The stability of silicon nanoparticles was examined using a separate software package, as stability analysis requires different computational methods compared to wavelength and absorption measurements. Table 5 presents the stability analysis of silicon nanoparticles, where the input parameters include aging time, laser energy, and the number of pulses. Each output parameter is influenced by different input parameters, ensuring a comprehensive evaluation of stability under varying conditions. The lower and upper aging time values are 1 and 3 months, respectively. The lower and upper values of the laser energy are 100 and 300 mJ, respectively. The lower and upper number of laser pulse values are 100 and 500 pulses, respectively. Moreover, the output parameter is the stability of Si NPs. A graphical representation of Table 4 is shown in Figure 8.

Figure 8 shows a three-dimensional graph of the high stability at 100–300 pulses. The max. and min. stability values were 31.43 and 19.08 mV, respectively. Large silicon nanoparticles were formed due to the aggregation effect when the laser energy was high with a low laser pulse number. The stability value decreased when the laser energy increased. Equation (5) is the quadratic equation that should be used to evaluate stability:

$$\begin{aligned} Z = {} & 47.5541 + (-8.2525)T + (-0.02702)E \\ & + (-0.01572)N + 0.0065T \times E \\ & + 0.0019625T \times N + 7.5 \times 10^{-6} \times E \times N \\ & + 0.5588T^2 + (-3.4875) \times 10^{-5} \times E^2 \\ & + (-4.15625) \times 10^{-6} \times N^2, \end{aligned} \quad (5)$$

where Z is the Zeta Potential [mv], T is the aging time [months], E is the laser energy [J], and N is the number of laser pulses.

The final regression equation was also an excellent way to predict and study how the parameters affect each other. The optimum values of the output parameters for Table 4 are shown in Figure 9.

Figure 9 shows the optimum value of the output response (stability) for silicon nanoparticles. When Nd:YAG laser was used, the optimum stability value was 33.5 mV.

3.5. Quartz microprocessing

3.5.1. Microlens fabrication

The fabrication of quartz microlens can be accomplished by two subsequent stages: material removal by fibre laser and the reshaping process by CO_2 laser. The parameters used in the Design Expert software

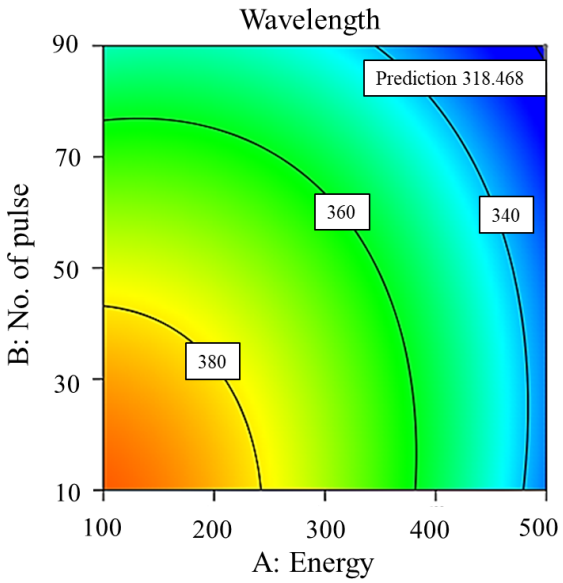

(a). Wavelength peak.

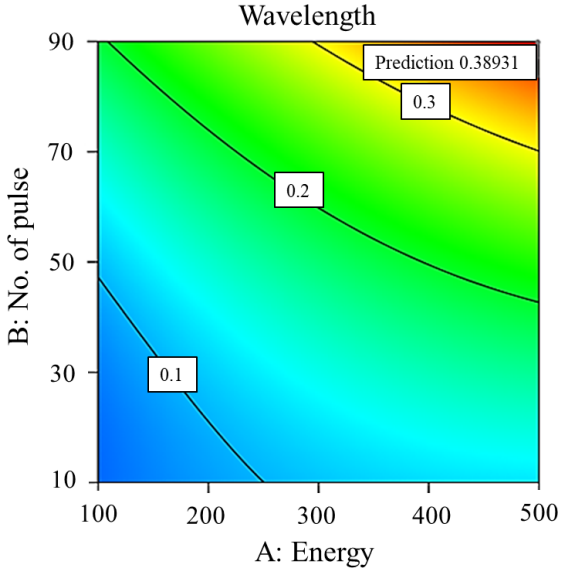

(b). Absorption peak.

Figure 7. The contour graph of optimum value for silicon NPs.

for the experimental stage are presented in Table 6. In this study, all input parameters, including power, speed, and count, were experimentally determined to analyse their influence on the output parameters, such as lens diameter, depth, focal point, $F^{\#}$, and NA. The software organises the experimental data, generates equations that establish relationships between the input and output parameters, and then performs an optimisation process to determine the most effective conditions.

Table 6 shows the experimental results of the quartz microlens fabrication. The input parameters were laser power, laser speed, and the number of repeated processes. The laser power lower and upper values are 10 and 20 W, respectively. The lower and upper values of the laser speed are 50 and 150 mm s^{-1}, respectively,

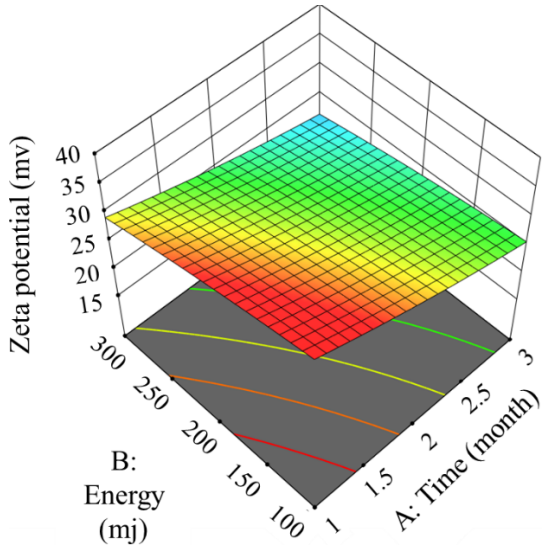

(A). No. of pulses: 100.

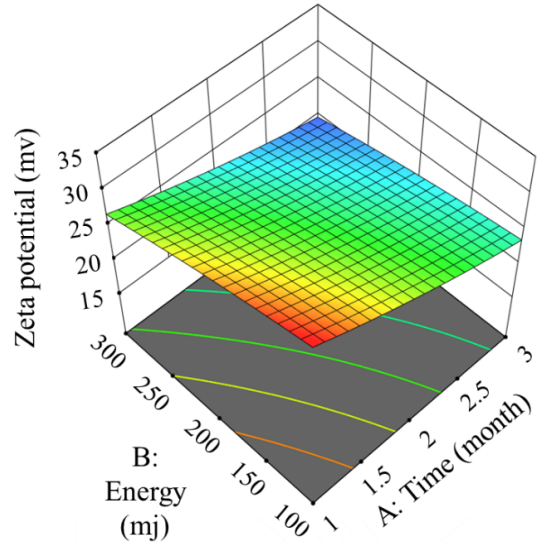

(B). No. of pulses: 300.

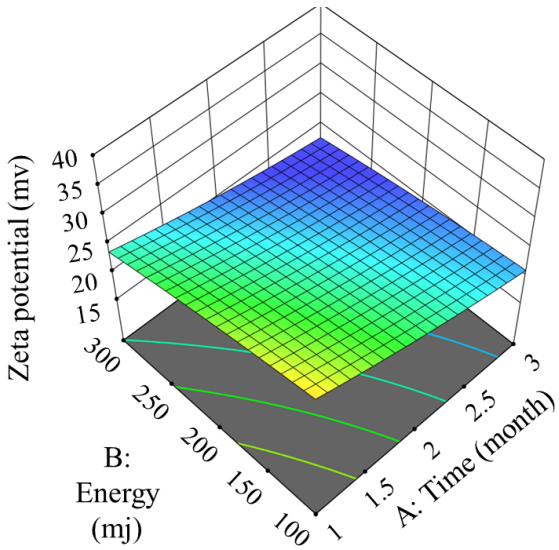

(C). No. of pulses: 500.

FIGURE 8. The stability curve for aging time and energy at No. of pulses: 100, 300, and 500.

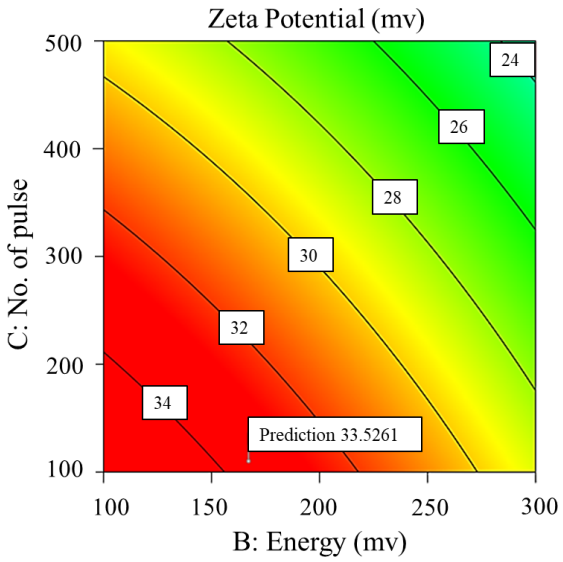

FIGURE 9. The contour graph of optimum value for stability.

while the number of repeated processes ranges from 1 to 9. the output parameters were the lens diameter, depth, focal length, $F^{\#}$, and numerical aperture. The f-number of a lens ($F^{\#}$) is a dimensionless number that expresses the ratio of the focal length (f) to the diameter of the entrance pupil. It controls the amount of light that enters the lens and affects the depth of field in imaging devices. The numerical aperture (NA) of a lens is a dimensionless metric that indicates its ability to collect light and resolve fine detail. A graphical representation of the numerical aperture, which is given in Table 6, is shown in Figure 10.

Figure 10 shows the three-dimensional graph of the microlens NA for one to nine times repeated processes. The max. and min. NA values were 0.108 and 0.543 mV, respectively. A deeper dip is produced when the laser power is increased and the laser speed is decreased, along with a higher number of repeated processes. This is due to an increase in ablated material and a greater numerical aperture (NA).

The quadric equation that should be used to evaluate the numerical aperture of quartz microlens is shown below:

$$\begin{aligned} \mathrm{NA} = {} & 0.5495 + 0.00054P + 0.0149S + 0.0073C \\ & + 0.0017P \times S + (-0.0002)P \times C \\ & + (-0.0145)S \times C + 0.0050P^2 \\ & + (-0.0125401)S^2 + (-0.0054)C^2 \\ & + (-0.0133)P^2 \times S, \end{aligned} \tag{6}$$

where P is the fibre laser power [P], S is the laser speed [mm s^{-1}], and C is the number of repeated processes.

The final regression equation was also an excellent way to predict and study how parameters affect each other.

Run	Input parameters			Output parameters				
	A: Power [W]	B: Speed [mm s^{-1}]	C: Count	Lens diameter [µm]	Depth [µm]	Focal point [µm]	F#	NA
1	15	100	5	446	154	433.560	0.972	0.514
2	15	100	5	445	155	431.268	0.969	0.516
3	15	50	9	190	590	550.27	2.897	0.173
4	10	100	1	720	70	1 746.75	2.426	0.206
5	15	50	1	320	420	437.229	1.366	0.366
6	20	150	5	350	205	322.173	0.92	0.543
7	20	50	5	130	657	603.119	4.639	0.108
8	10	150	5	775	91	1 582.79	2.042	0.245
9	20	100	9	150	297	287.218	1.915	0.261
10	15	150	9	595	175	618.864	1.04	0.48
11	15	100	5	446	154	433.560	0.972	0.514
12	15	100	5	445	155	431.268	0.969	0.516
13	10	50	5	382	470	497.836	1.303	0.384
14	10	100	9	470	145	478.056	1.017	0.492
15	20	100	1	210	240	259.943	1.238	0.404
16	15	100	5	444	156	429.021	0.966	0.517
17	15	150	1	705	91	1 324.05	1.878	0.266

TABLE 6. Effects of laser power, laser speed, and No. of repeated processes on the lens diameter, lens depth, focal point, $F^{\#}$, and NA as determined by the DOE software.

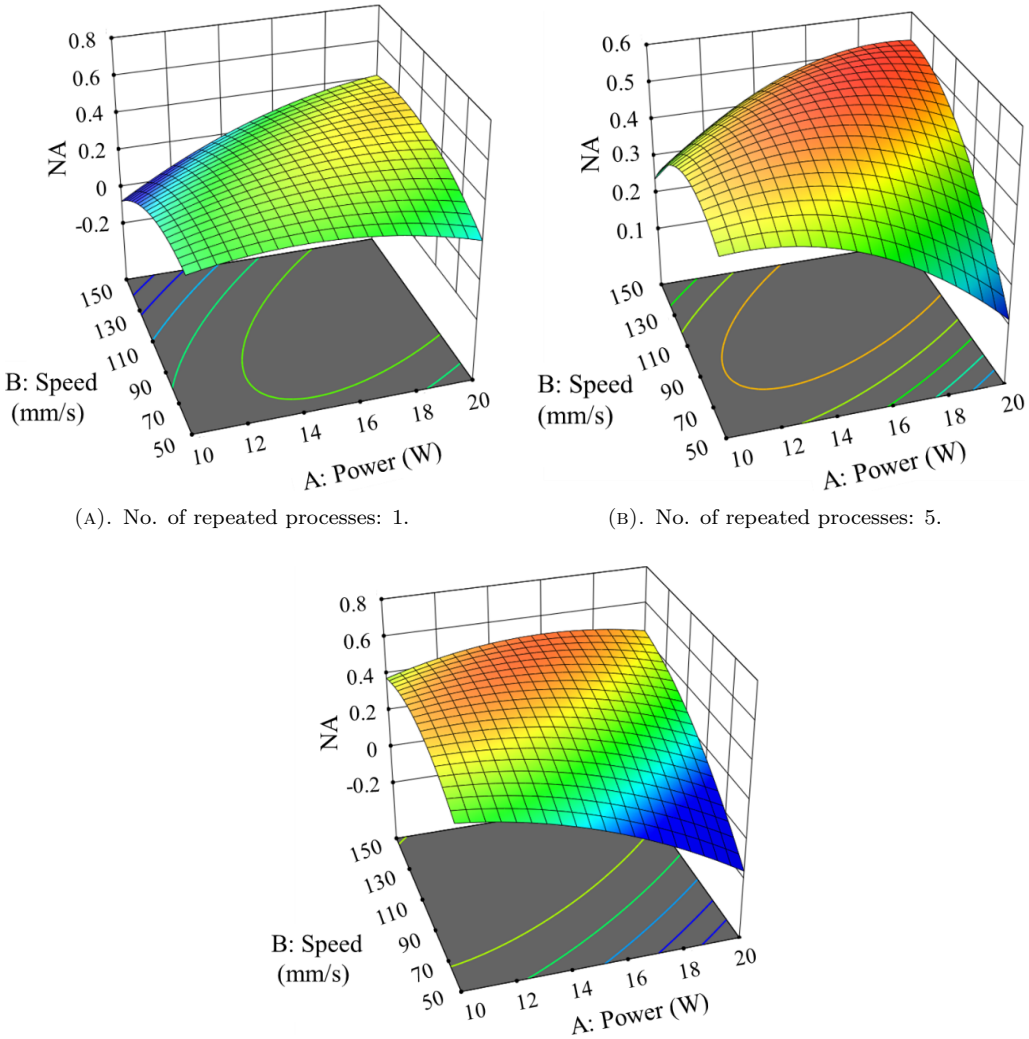

(A). No. of repeated processes: 1.

(B). No. of repeated processes: 5.

(C). No. of repeated processes: 9.

FIGURE 10. The NA 3D curve for laser power and laser speed at No. of repeated processes: 1, 5, and 9 times.

Run	Input parameters			Output parameter
	A: Power [W]	B: Speed [mm s^{-1}]	C: Count	Roughness [nm]
1	4	3	3	12.3
2	4	3	3	12.2
3	4	1	5	6.7
4	3	3	1	85.1
5	4	1	1	13.4
6	5	5	3	11.9
7	5	1	3	5.2
8	3	5	3	70.5
9	5	3	5	6.7
10	4	5	5	12.1
11	4	3	3	12.4
12	4	3	3	12.2
13	3	1	3	57.1
14	3	3	5	47
15	5	3	1	13.2
16	4	3	3	12.1
17	4	5	1	22.8

TABLE 7. Effects of laser power, laser speed, and No. of repeated processes on the lens diameter, lens depth, focal point, $F^{\#}$, and NA as measured by the DOE software.

3.5.2. MICROLENS ENHANCEMENT

Using the CO_2 laser during the reshaping stage is of considerable importance for enhancing the quality of microlenses. Table 7 presents the parameters of this stage, which were determined using the Design of Expert software for the experimental strategy. All input parameters, including laser power, laser speed, and the number of repeated processes, were experimentally determined to analyse their influence on the output parameter, which is lens roughness.

The laser power has lower and upper values of 3 and 5 W, respectively. The lower and upper values of the laser speed are 1 and 5 mm s^{-1}, respectively, while the number of repeated processes ranges from 1 to 5. The software organises the experimental data, generates equations that establish the relationship between the input parameters and lens roughness, and then performs the optimisation process to determine the most effective conditions. A graphical representation of the results in Table 7 is shown in Figure 11.

Figure 11 shows a three-dimensional graph of the lens height at one-fifth of the process. The max. and min. roughness values were 5 and 85 nm, respectively. When the laser power reached a high level, the laser speed decreased, and the number of repeated processes increased, resulting in the complete melting of the surface. This occurred because the laser power exceeded the melting point of the quartz material. Furthermore, it was observed that there was an increase in the roughness value as the laser speed increased.

The quadric equation that should be used to evaluate the roughness of quartz microlens is shown below:

$$\begin{aligned} R = {} & 12 + (-28)P + 4.25S + (-7.75)C + (-1.75)P \\ & \times S + 7.75P \times C + (-0.75) \times S \times C \\ & + 24.125P^2 + (-0.375)S^2 + 1.625C^2, \end{aligned} \tag{7}$$

where R is the roughness [nm], P is the CO_2 laser power [W], S is the laser speed [mm s^{-1}], and C is the repeated processes.

The final regression equation was also an excellent way to predict and study how the parameters affect each other.

The optimum values of the output parameters for Tables 5 and 6 are shown in Figure 12.

Figure 12 shows the optimum values of the output response for the quartz microlens. The optimum NA and roughness values were 0.494 and 4.5 nm, respectively.

4. CONCLUSION

This study used expert analysis software to optimise the parameters of laser micro/nano processing. The COMSOL software simulation was used to analyse the thermal distribution on the surface and in the area beneath the surface of silicon wafers and quartz sheets under laser irradiation. Using the Nd:YAG laser, fibre laser, and CO_2 laser in micro/nano machining of silicon and quartz resulted in the formation of stable silicon nanoparticles and the creation of a quartz microlens array. Furthermore, the numerical optimisation using the DOE software yielded silicon nanoparticles with desired properties and quartz microlenses with specific dimensions and characteristics. The optimal parameter for silicon NPs (stability) was 33 mV, while for quartz microlenses (NA and roughness), it was 0.494 and 4.5 nm, respectively. Finally, the controllable laser micro/nano machining process demonstrated the potential applications of silicon nanoparticles and quartz microlenses in optoelectronics and biological imaging, which can benefit from the unique features offered by these lenses. Future endeavours

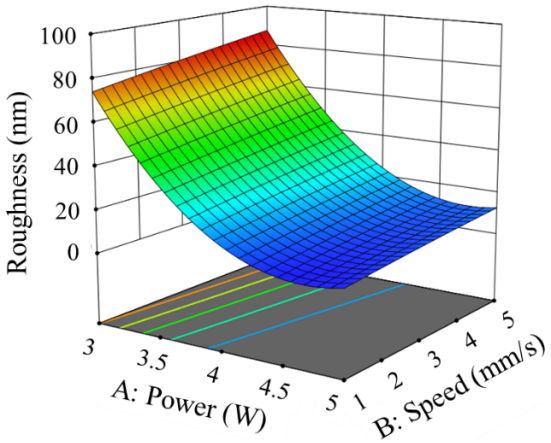

(A). No. of repeated processes: 1.

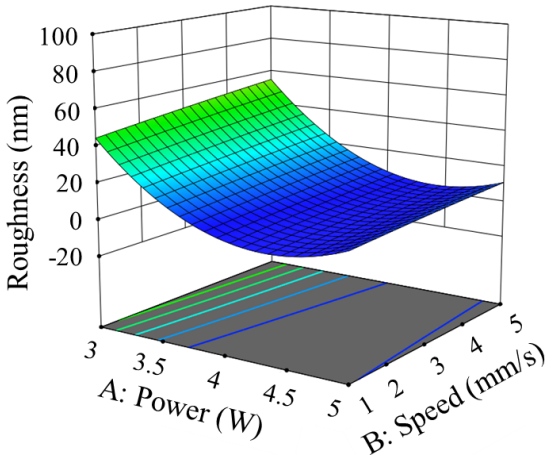

(B). No. of repeated processes: 3.

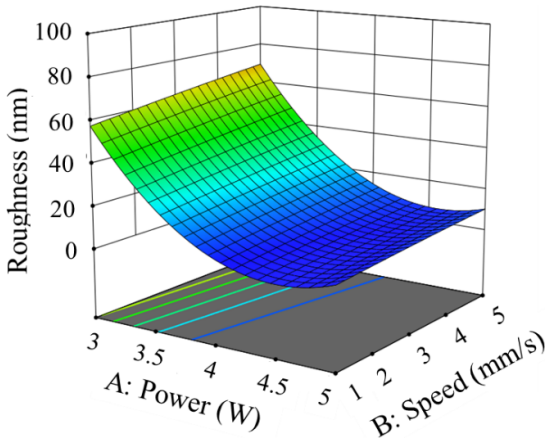

(C). No. of repeated processes: 5.

Figure 11. The roughness 3D curve for laser power and laser speed at No. of repeated processes: 1, 3, and 5 times.

should focus on further parameter optimisation for laser microprocessing, investigating alternative materials and scalable production methods. The aim is to improve precision engineering, increase the versatility of materials, and enable the real-world application of silicon nanoparticles and quartz microlenses for various purposes.

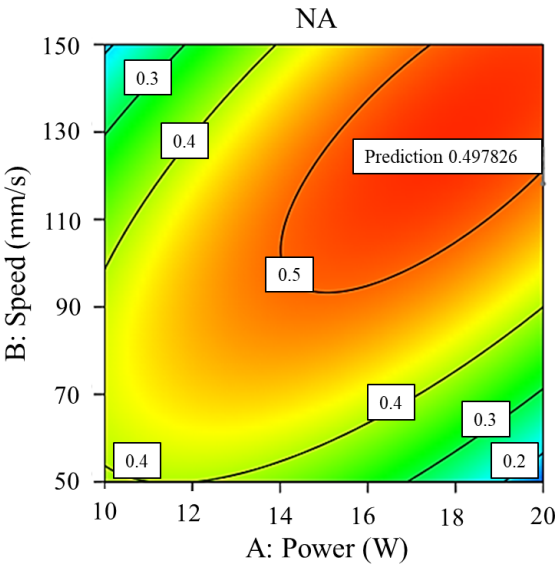

(A). NA.

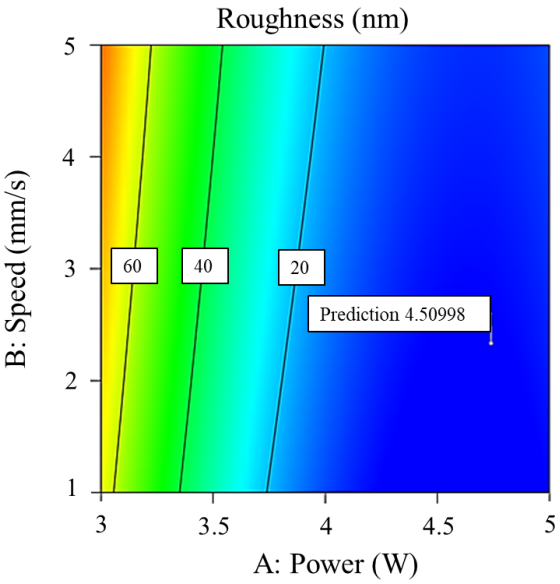

(B). Roughness.

Figure 12. The contour graph of optimum value for: NA and roughness.

References

[1] L. Rihakova, H. Chmelickova. Laser micromachining of glass, silicon, and ceramics. A review. *European International Journal of Science and Technology* **4**(7):41–49, 2015.

[2] J. Wang, F. Fang, H. An, et al. Laser machining fundamentals: micro, nano, atomic and close-to-atomic scales. *International Journal of Extreme Manufacturing* **5**(1):012005, 2023. https://doi.org/10.1088/2631-7990/acb134

[3] S. N. Grigoriev, M. A. Volosova, A. A. Okunkova. Advances in laser materials processing. *Metals* **12**(6):917, 2022. https://doi.org/10.3390/met12060917

[4] H. Minghui. Laser-material interaction and its applications in surface micro/nanoprocessing. *AIP Conference Proceedings* **1278**(1):293–302, 2010. https://doi.org/10.1063/1.3507115

[5] F. A. Lasagni, A. F. Lasagni (eds.). *Fabrication and characterization in the micro-nano range*. Advanced Structured Materials. Springer Berlin, Heidelberg, Germany, 2011. https://doi.org/10.1007/978-3-642-17782-8

[6] W. A. Ghaly, H. T. Mohsen. Laser-induced silicon nanocolumns by ablation technique. *Journal of Radiation Research and Applied Sciences* **13**(1):398–405, 2020. https://doi.org/10.1080/16878507.2020.1740395

[7] M. J. Mahmoud, B. G. Rasheed. Synthesis of nano silicon using lasers. *International Journal of Nanoelectronics and Materials* **17**(1):28–34, 2024. https://doi.org/10.58915/ijneam.v17i1.449

[8] C. Gaudiuso, A. Volpe, A. Ancona. Single-pass direct laser cutting of quartz by IR femtosecond pulses. In U. Klotzbach, A. Watanabe, R. Kling (eds.), *Laser-based Micro- and Nanoprocessing XV*, vol. 11674, p. 116740E. International Society for Optics and Photonics, SPIE, 2021. https://doi.org/10.1117/12.2577177

[9] T. D. Sherpa, B. B. Pradhan. Micro-grooving of silicon wafer by Nd:YAG laser beam machining. *IOP Conference Series: Materials Science and Engineering* **377**(1):012219, 2018. https://doi.org/10.1088/1757-899X/377/1/012219

[10] I. Sopyan, D. Gozali, S. Sriwidodo, R. K. Guntina. Design-expert software (DOE): An application tool for optimization in pharmaceutical preparations formulation. *International Journal of Applied Pharmaceutics* **14**(4):55–63, 2022. https://doi.org/10.22159/ijap.2022v14i4.45144

[11] R. Tewari, M. K. Singh, S. Zafar, S. Powar. Parametric optimization of laser drilling of microwave-processed kenaf/HDPE composite. *Polymers and Polymer Composites* **29**(3):176–187, 2021. https://doi.org/10.1177/0967391120905705

[12] S. Theeda, B. B. Ravichander, S. H. Jagdale, G. Kumar. Optimization of laser process parameters using machine learning algorithms and performance comparison. In *Proceedings of the 33rd Annual International Solid Freeform Fabrication Symposium*, pp. 1581–1592. 2022. https://doi.org/10.26153/tsw/44608

[13] Z. Zheng, Y. Ma, Z. Wang, et al. Dual-method characterization and optimization of drilling parameters for picosecond laser drilling quality in CFRP. *Polymers* **16**(18):2603, 2024. https://doi.org/10.3390/polym16182603

[14] A. R. A. Aziz, S. A. Aziz. Application of Box Behnken design to optimize the parameters for Kenaf-epoxy as noise absorber. *IOP Conference Series: Materials Science and Engineering* **454**(1):012001, 2018. https://doi.org/10.1088/1757-899X/454/1/012001

[15] R. Intartaglia, K. Bagga, M. Scotto, et al. Luminescent silicon nanoparticles prepared by ultra short pulsed laser ablation in liquid for imaging applications. *Optical Materials Express* **2**(5):510–518, 2012. https://doi.org/10.1364/OME.2.000510

[16] W. R. Runyan. *Silicon semiconductor technology*. McGraw-Hill, New York, USA, 1965.

[17] M. B. Larosi, J. del V. García, A. R. Rodríguez. Laser synthesis of nanomaterials. *Nanomaterials* **12**(17):2903, 2022. https://doi.org/10.3390/nano12172903

[18] M. J. Mahmoud, B. G. Rasheed. Fabrication of quartz microlenses using laser ablation. *Instrumentation Science & Technology* **52**(6):637–646, 2024. https://doi.org/10.1080/10739149.2024.2305198

[19] P. Chewchinda, T. Tsuge, H. Funakubo, et al. Laser wavelength effect on size and morphology of silicon nanoparticles prepared by laser ablation in liquid. *Japanese Journal of Applied Physics* **52**(2R):025001, 2013. https://doi.org/10.7567/JJAP.52.025001

[20] M. J. Mahmoud, B. G. Rasheed, M. M. Hanon. Optimization of laser micro/nano processing of silicon and quartz. *International Journal of Nanoelectronics and Materials* **17**(June):93–100, 2024. https://doi.org/10.58915/ijneam.v17iJune.840

[21] L. A. J. Garvie, P. Rez, J. R. Alvarez, et al. Bonding in alpha-quartz (SiO_2): A view of the unoccupied states. *American Mineralogist* **85**(5–6):732–738, 2000. https://doi.org/doi:10.2138/am-2000-5-611

[22] H. K. Hasan. Analysis of the effecting parameters on laser cutting process by using response surface methodology (RSM) method. *Journal of Achievements in Materials and Manufacturing Engineering* **110**(2):59–66, 2022. https://doi.org/10.5604/01.3001.0015.7044

[23] J. Wu, C. Zhang, P. Jiang, et al. A prediction approach of fiber laser surface treatment using ensemble of metamodels considering energy consumption and processing quality. *Green Manufacturing Open* **1**(1):3, 2023. https://doi.org/10.20517/gmo.2022.04

[24] D. Leahu, C. Petrianu, G. Nagit. Quality control and optimization of a laser cutting system for cutting 10 mm mild steel using DOE software. *International Journal of Modern Manufacturing Technologies* **8**(1):7–11, 2016.

[25] S. Singh, N. Yaragatti, M. Doddamani, et al. Drilling parameter optimization of cenosphere/HDPE syntactic foam using CO_2 laser. *Journal of Manufacturing Processes* **80**:28–42, 2022. https://doi.org/10.1016/j.jmapro.2022.05.040

[26] D. Teixidor, I. Ferrer, J. Ciurana, T. Özel. Optimization of process parameters for pulsed laser milling of micro-channels on AISI H13 tool steel. *Robotics and Computer-Integrated Manufacturing* **29**(1):209–218, 2013. https://doi.org/10.1016/j.rcim.2012.05.005